Three-dimensional, multifluid, high spatial resolution MHD model studies of the solar wind interaction with Mars

Dalal Najib,[1] Andrew F. Nagy,[1] Gábor Tóth,[1] and Yingjuan Ma[2]

Received 5 November 2010; revised 7 February 2011; accepted 9 February 2011; published 10 May 2011.

[1] Our newly developed 3-D, multifluid MHD model is used to study the interaction of the solar wind with Mars. This model is based on the BATS-R-US code, using a spherical grid and a radial resolution equal to 10 km in the ionospheric regions. We solve separate continuity, momentum, and energy equations for each ion fluid and run our model for both solar minimum and maximum conditions. We obtain asymmetric densities, velocities, and magnetic pileup in the plane containing both the direction of the solar wind and the convective electric field. These asymmetries are the result of the decoupling of the individual ions; therefore, our model is able to account for the respective dynamics of the ions and to show new physical processes that could not be observed by the single-fluid model. Our results are consistent with the measured bow shock and magnetic pileup locations and with the Viking-observed ion densities. We also compute the escape fluxes for both solar minimum and solar maximum conditions and compare them to the single-fluid results and the observed values from Mars Express.

Citation: Najib, D., A. F. Nagy, G. Tóth, and Y. Ma (2011), Three-dimensional, multifluid, high spatial resolution MHD model studies of the solar wind interaction with Mars, *J. Geophys. Res.*, *116*, A05204, doi:10.1029/2010JA016272.

1. Introduction

[2] In this paper we describe our new 3-D, multifluid, MHD model and compare the results with the relevant and available data, in order to help us elucidate some of the physics involved in these interactions. This new model is the next logical step in our approach of incremental improvements, as computational resources increase. This gradual approach is also very useful in checking and validating these complex computational schemes.

[3] Model studies of the interaction of fast moving plasmas with nonmagnetic solar system bodies go back quite a few decades. These interactions are very different from those with bodies that have strong magnetic fields, such as the Earth or Jupiter, because the obstacle to the supersonic solar wind flow is the ionosphere/atmosphere system, not the intrinsic magnetic field. Over the years many models have been developed and used to study the interactions with these nonmagnetized planets: gasdynamic [e.g., *Spreiter et al.*, 1970], single-fluid MHD [e.g., *Tanaka and Murawski*, 1997; *Bauske et al.*, 1998; *Ma et al.*, 2004, 2007; *Terada et al.*, 2009], multifluid MHD [*Harnett and Winglee*, 2003, 2007], and semikinetic (hybrid) [e.g., *Brecht*, 1997; *Brecht and Ledvina*, 2007; *Modolo et al.*, 2006; *Simon et al.*, 2007; *Kallio et al.*, 2010]. Both the MHD and hybrid models have their strengths and weaknesses, which have been well known and discussed before [e.g., *Ledvina et al.*, 2008; *Brain et al.*, 2010], thus this will be discussed only briefly here. MHD models are based on fluid assumptions and thus where the ion gyroradius is of the same order as the planetary radius their applicability has been questioned. However, significant wave activity and turbulence, which are usually present, lead to a wide variety of wave particle interactions, which in turn act as pseudocollisions. Also, it should be remembered that the interplanetary/planetary magnetic field piles up near the body, thus reducing the gyroradius. Finally, the introduction of the Hall effect and multifluid formulation, are important steps in overcoming these limitations. The main difficulty with the semikinetic (hybrid) models has been their limited spatial resolution, caused mainly by limited computing resources.

2. Model Description

[4] Our previous multispecies model had continuity equations for all the ions, but only one momentum and one energy equation. In the case of multifluid formulation, we have separate mass, momentum and energy equations for the four fluids H^+, O_2^+, O^+, CO_2^+ (and in one case we consider five separate fluids by separating the solar wind and ionospheric H^+). The multi-ion MHD equations can be written in nonconservative form only and are as follows:

$$\frac{\partial \rho_s}{\partial t} + \nabla \cdot (\rho_s \mathbf{u}_s) = S_{\rho_s}, \tag{1}$$

[1]Department of Atmospheric, Oceanic and Space Sciences, University of Michigan, Ann Arbor, Michigan, USA.
[2]Institute of Geophysics and Planetary Physics, University of California, Los Angeles, California, USA.

0148-0227/11/2010JA016272

Table 1. Reactions, Ionization Frequencies, and Rates Considered in the Model

Reactions	Ionization Frequency and Rate Coefficient	References
$CO_2 + h\nu \rightarrow CO_2^+ + e$	$7.30 \times 10^{-7}\ s^{-1}$ (*solarmax*) $2.47 \times 10^{-7}\ s^{-1}$ (*solarmin*)	*Schunk and Nagy* [2009]
$O + h\nu \rightarrow O^+ + e$	$2.73 \times 10^{-7}\ s^{-1}$ (*solarmax*) $8.89 \times 10^{-8}\ s^{-1}$ (*solarmin*)	*Schunk and Nagy* [2009]
$H + h\nu \rightarrow H^+ + e$	$8.59 \times 10^{-8}\ s^{-1}$ (*solarmax*) $5.58 \times 10^{-8}\ s^{-1}$ (*solarmin*)	*Ma et al.* [2004]
$CO_2^+ + O \rightarrow O_2^+ + CO$	$1.64 \times 10^{-10}\ cm^{-3}\ s^{-1}$	*Schunk and Nagy* [2009]
$CO_2^+ + O \rightarrow O^+ + CO_2$	$9.60 \times 10^{-11}\ cm^{-3}\ s^{-1}$	*Schunk and Nagy* [2009]
$O^+ + CO_2 \rightarrow O_2^+ + CO$	$1.1 \times 10^{-9}(\frac{800}{Ti})^{(0.39)}\ cm^{-3}\ s^{-1}$	*Fox and Sung* [2001]
$O^+ + H \rightarrow H^+ + O$	$6.4 \times 10^{-10}\ cm^{-3}\ s^{-1}$	*Schunk and Nagy* [2009]
$H^+ + O \rightarrow O^+ + H$	$5.08 \times 10^{-10}\ cm^{-3}\ s^{-1}$	*Fox and Sung* [2001]
$O_2^+ + e \rightarrow O + O$	$7.38 \times 10^{-8}(\frac{1200}{Te})^{(0.56)}\ cm^{-3}\ s^{-1}$	*Schunk and Nagy* [2009]
$CO_2^+ + e \rightarrow CO + O$	$3.10 \times 10^{-7}(\frac{300}{Te})^{(0.5)}\ cm^{-3}\ s^{-1}$	*Schunk and Nagy* [2009]

$$\frac{\partial \rho_s \mathbf{u}_s}{\partial t} + \nabla \cdot (\rho_s \mathbf{u_s} \mathbf{u_s} + I p_s) = n_s q_s (\mathbf{u}_s - \mathbf{u}_+) \times \mathbf{B} + \frac{n_s q_s}{n_e e}(\mathbf{J} \times \mathbf{B} - \nabla p_e) + S_{\rho_s} u_s, \quad (2)$$

$$\frac{\partial p_s}{\partial t} + \nabla \cdot (p_s \mathbf{u}_s) = -(\gamma - 1) p_s (\nabla \cdot \mathbf{u}_s) + S_{p_s}, \quad (3)$$

where ρ_s, n_s, q_s, $\mathbf{u}_s$ and p_s are the individual mass density, number density, charge, velocity and pressure of the ions, respectively. **B** is the magnetic field, **J** is the current density, I is the identity matrix, e is the electric charge and γ is the ratio of specific heats (and taken to be $\frac{5}{3}$).

[5] As for the induction equation, it can be written either without the Hall term,

$$\frac{\partial B}{\partial t} - \nabla \times (\mathbf{u}_+ \times \mathbf{B}) = 0, \quad (4)$$

or including the Hall term,

$$\frac{\partial B}{\partial t} - \nabla \times (\mathbf{u}_e \times \mathbf{B}) = 0, \quad (5)$$

where $\mathbf{u}_e = \mathbf{u}_+ - \frac{\mathbf{J}}{ne}$. We made runs for both cases.

[6] The electron number density n_e can be calculated from charge neutrality as

$$n_e = \frac{1}{e} \sum_s n_s q_s. \quad (6)$$

[7] The charge averaged ion velocity $\mathbf{u}_+$ is

$$\mathbf{u}_+ = \frac{\sum_s n_s q_s \mathbf{u}_s}{e n_e}. \quad (7)$$

[8] At this time, we do not solve the electron pressure equation, but take the electron pressure gradient term in the momentum equation to be equal to the total ion pressure gradient.

[9] As for the source terms S_{ρ_s}, the mass density source term, $S_{\rho_s u_s}$, the momentum source term and S_{ρ_s}, the pressure source term, they contain charge exchange, photoionization, recombination, ion-neutral and ion-ion collisions:

$$S_{\rho_s} = S_s - L_s, \quad (8)$$

$$S_{\rho_s u_s} = \rho_s g - \rho_s \sum_{t=neutrals} \nu_{st}(u_n - u_s) + S_s u_n - L_s u_s, \quad (9)$$

$$S_{p_s} = 2 \sum_{t=neutrals} \nu_{st} \frac{m_s}{m_s + m_t} n_s k (T_n - T_s) + 2 \times \sum_{t=ions} \nu_{st} \frac{m_s}{m_s + m_t} n_s k (T_t - T_s) + \frac{2}{3} \sum_{t=neutrals} \nu_{st} \frac{m_s m_t}{m_s + m_t} n_s (u_n - u_s)^2 + k \frac{S_s T_n - L_s T_s}{m_s} + \frac{1}{3} S_s (u_n - u_s)^2 + \frac{n_s}{n_e} k \frac{S_e T_n - L_e T_e}{m_e}, \quad (10)$$

with S_s and L_s, the production and loss rate for ions, S_e and L_e, the production and loss rate for electrons, respectively, T_s and m_s, the ion temperature and mass, T_n and u_n are the neutral temperature and velocity, m_e, the electron mass, k is the Boltzmann constant and ν_{st} is the collision frequency between species s and t.

[10] We use a reasonably comprehensive chemical scheme; the associated ionization frequencies, reactions and rates are presented in Table 1. For the photoionization of the neutral species, we use different ionization frequencies (corresponding to the unattenuated flux) for solar minimum and maximum conditions. In order to evaluate some of the reaction rates that are temperature dependent, the individual ion temperatures are obtained from the individual pressures, while the electron temperature is assumed to be equal to the average ion temperature.

[11] It is important to point out that in our multifluid simulations, the addition of ion-ion collisions has considerably improved our results, in particular our fit to the data. We choose to include ion-ion collisions since they are not negligible in the lower ionosphere, where they contribute to the pressure source term and bring the individual ion temperatures closer to one another. We neglected the friction term resulting from ion-ion collisions since in this region of interest, the ion velocities are small.

[12] We approximate the optical depth effect by including a cosine factor for the different solar zenith angles and by assuming average absorption coefficients of 2.6×10^{-17} and 1.5×10^{-17} cm^2 for CO_2 and O, respectively [*Schunk and Nagy*, 2009]. On the nightside, we set the solar flux to be 10^{-15} times the unattenuated solar radiation, so as to avoid

Table 2. Simulation Cases Used in This Study

Simulation Cases	Solar Condition	Upstream B Field	Subsolar Position
Case 1	Solar minimum (test case)	symmetric B field (0, 3 nT, 0)	no crustal field
Case 2	Solar minimum	3nT Parker spiral	no crustal field
Case 3	Solar minimum	3nT Parker spiral	99.4° W 25.3° N
Case 4	Solar maximum	3nT Parker spiral	180° W 0° N

zeros. In order to permit direct comparison with the multispecies model results we select the neutral atmosphere to be the same as was used by *Ma et al.* [2004].

[13] We run simulations with and without crustal fields and also for the solar minimum and maximum condition. We use the 60 degree harmonic expansion for the crustal magnetic field developed by *Arkani-Hamed* [2001] to describe the observed fields at Mars [*Acuna et al.*, 1998].

3. Numerical Implementation

[14] Our new multifluid model, to be presented here, evolved from our 3-D, spherical, multispecies MHD model [*Ma et al.*, 2004]; the Hall term was added a few years ago [*Ma et al.*, 2007; *Tóth et al.*, 2008]. This model is implemented into the BATS-R-US (Block Adaptive-Tree Solar wind Roe-type Upwind Scheme) code [cf. *Powell et al.*, 1999; *Tóth et al.*, 2011], developed for space physics application at the University of Michigan. The implementation of an appropriate numerical approach to solving these multifluid equations is not without significant challenges. New algorithms were implemented to address several issues, in particular stability, positivity and conservation.

[15] Stability problems are essentially due to stiff source terms. In order to maintain stability, while taking large enough time steps, the stiff terms are treated in a point-implicit manner [*Glocer et al.*, 2009; *Tóth et al.*, 2009].

[16] As for conservation, it is essential to use a conservative discretization to capture shocks correctly. Unfortunately the multi-ion MHD equations cannot be written in conservative form, therefore a conservative discretization is not possible. However, we can solve the multi-ion energy equations conservatively in the hydrodynamic limit, when the magnetic energy density and ∇p_e are small relative to the kinetic and thermal terms. We therefore solve for the energy density $e_s = \rho_s\, \mathbf{u}_s^2/2 + p_s/(\gamma - 1)$ as

$$\frac{\partial e}{\partial t} + \nabla \cdot [(e_s + p_s)\mathbf{u_s}] = \mathbf{u_s} \cdot \left[\frac{n_s q_s}{n_e e}(\mathbf{J} \times \mathbf{B} - \nabla p_e) + n_s q_s(\mathbf{u_s} - u_+) \times \mathbf{B}\right] + S_{e_s}, \quad (11)$$

where S_{es} is the energy source term. We only apply the conservative discretization outside and around the bow shock, where this approximation is appropriate.

[17] In the case of Mars, the most important numerical challenge has been to maintain the positivity of pressure and density of all ion fluids. In the regions upstream of the body where the plasma consists essentially only of solar wind protons, the ionospheric ion densities are initialized to very small values (a fraction of the total density $\sim 10^{-9}$), while velocity and temperature are set to the same value as the total fluid, in order to avoid zeros and associated problems. The issue of positivity also arises when implementing a conservative scheme. At times we may obtain negative values for the thermal pressure when we compute it by subtracting the kinetic energy from the hydrodynamic energy. In order to solve this problem, we check the pressures at every time step and if it is negative we overwrite it by a very small fraction of the total pressure.

[18] The X axis of our coordinate system points from Mars toward the Sun, the Z axis is normal to Mars' orbital plane and positive toward the north celestial pole, and the Y axis completes the right-hand coordinate system. Our computational domain is defined by $-24R_M \le X \le 8R_M$, $-16R_M \le Y,\ Z \le 16R_M$, where R_M is the radius of Mars ($\sim$ 3396 km). We use a nonuniform, spherical grid structure with a radial resolution varying from 10 km at the lower boundary to 630 km at the outer boundary.

[19] We set our lower boundary to 100 km above the surface. The O_2^+, O^+ and CO_2^+ densities at the inner boundary are taken to be the photochemical equilibrium values, H^+ density is set to be approximately zero. The electron and ion temperatures are assumed to be equal to the neutral temperature. A reflective boundary condition is used for **u** that results in near zero velocities at the inner boundary. We ran our model for the four different cases presented in Table 2. Cases 1 and 2 are idealized simulations to better understand the model. Cases 3 and 4 correspond to realistic cases (solar minimum and maximum, respectively). The upstream solar wind ion and electron temperatures are set to 5×10^4 and 3×10^5 K, respectively. The IMF (Interplanetary Magnetic Field) is assumed to be a Parker spiral in the X-Y plane with an angle of 56 degrees and a magnitude of 3 nT (except for case 1, where the IMF has only a By component). The solar wind velocity and density are selected to be 400 km/ s and 4 cm^{-3}, respectively, for all the simulated cases.

4. Simulation Results and Discussion

[20] We first look at the symmetric test case (case 1) results for both single and multifluid cases. The O_2^+ ion densities in the X-Z plane are shown in Figure 1. These ions are generated by charge exchange from O^+ and CO_2^+ (see Table 1). While in the single-fluid case the O_2^+ ion distribution is symmetric, in the multifluid MHD case, O_2^+ ions can move upstream and across the dominant H^+ ions of the solar wind. The density distribution is asymmetric due to the effect of the convective electric field **E** (along the Z axis, pointing northward), accounted for in the multifluid momentum equation, unlike the single-fluid case.

[21] In fact, the main signature of multifluid effects are the asymmetries due to the Lorentz force on each ion. In the individual momentum equation, we include the gyration of the ion with respect to the charge averaged velocity ($\mathbf{u_s} - \mathbf{u}_+$). It can easily be proved that ($\mathbf{u_s} - \mathbf{u}_+$) × **B** term will lead to an asymmetry in the X-Z plane only, as long as the magnetic

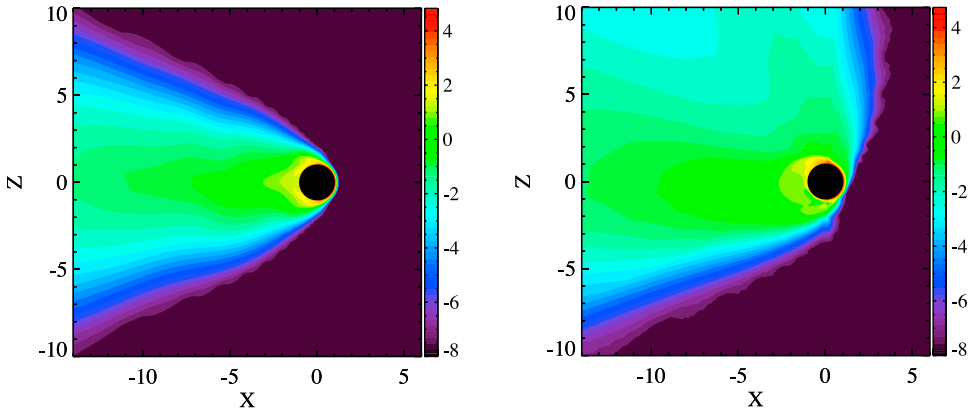

Figure 1. Calculated O_2^+ number densities from the (left) single-fluid and (right) multifluid models in a logarithmic scale from 10^{-8} to over 10^4 cm^{-3} (case 1).

field is in the X-Y plane. In Figures 2 and 3 we show the calculated magnetic field and velocity values for solar minimum conditions, without crustal fields. We do this in order to show clearly the signature of the multifluid effects. In both Figures 2 and 3, we plotted the magnetic field in the X-Y and X-Z planes, respectively. The magnetic field in the X-Z plane is clearly asymmetric. This is a very important signature that we could not observe with ideal single-fluid MHD.

[22] In the X-Y plane, the magnetic pileup is symmetric (Figure 3). However, the shock position on the dawn side is closer than the shock position at the duskside. This confirms previous results of the single-fluid model [*Ma et al.*, 2004]. In fact, quasi-perpendicular shocks are dominating in the duskside, while quasi-parallel shocks dominate in the dawnside. Moreover, based on MGS observations [*Vignes et al.*, 2002], quasi-parallel shocks are closer to the planet than the quasi-perpendicular shocks.

[23] Similarly, the velocity profiles in Figures 2 and 3 show a sharp asymmetry in the X-Z plane and a symmetry in the X-Y plane. The newly observed asymmetry is again absent in the single-fluid case [*Ma et al.*, 2004]. The asymmetry of the total velocity in the X-Z plane is a result of the asymmetry of the individual velocities, since the total momentum is the sum of the individual momenta.

4.1. Density

[24] The multifluid effect can also be seen in the density results. Again, while in the single-fluid case the densities are symmetric, the multifluid densities are strongly asymmetric in the X-Z plane as we can see it in Figure 4.

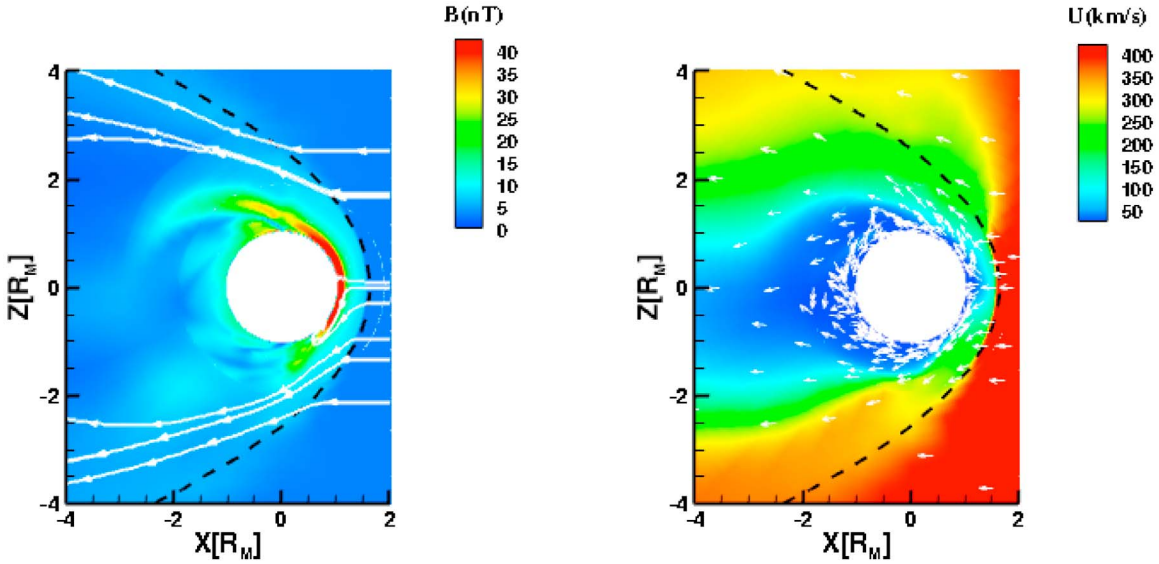

Figure 2. The calculated magnetic field and average ion velocity in the meridional plane in the X-Z plane for solar minimum conditions. The color plots show the magnitudes; the white lines marked with arrows indicate the vector direction of the magnetic field; and the white arrows show the direction (not the magnitude) of the velocity (case 2). The dashed line represents the mean bow shock location from *Vignes et al.* [2000].

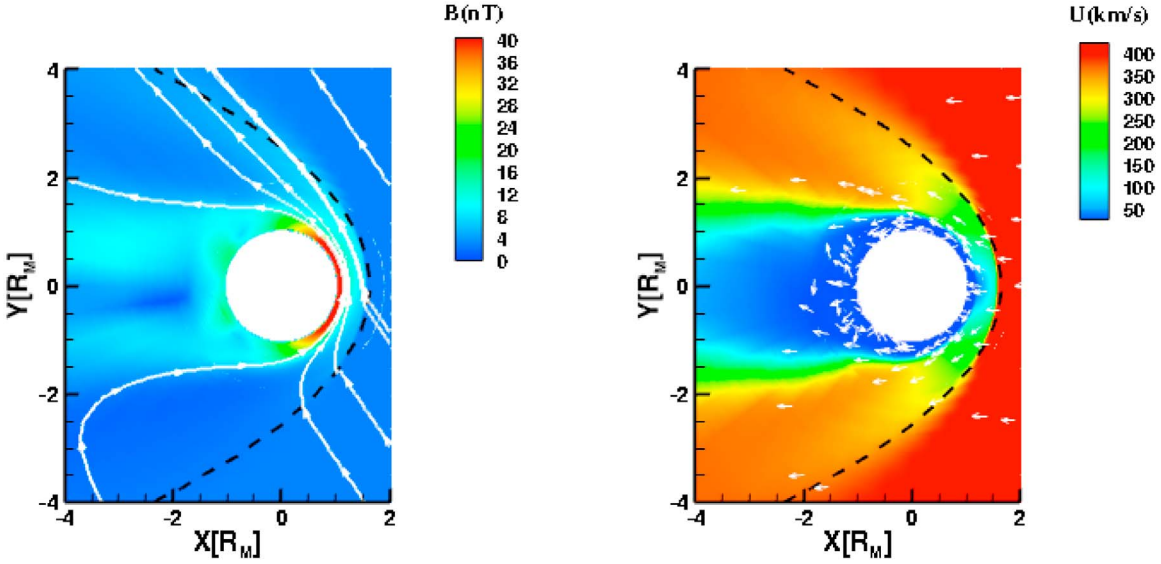

Figure 3. The calculated magnetic field and average ion velocity in the equatorial plane in the X-Y plane for solar minimum conditions. The color plots show the magnitudes; the white lines marked with arrows indicate the vector direction of the magnetic field; and the white arrows show the direction (not the magnitude) of the velocity (case 2). The dashed line represents the mean bow shock location from *Vignes et al.* [2000].

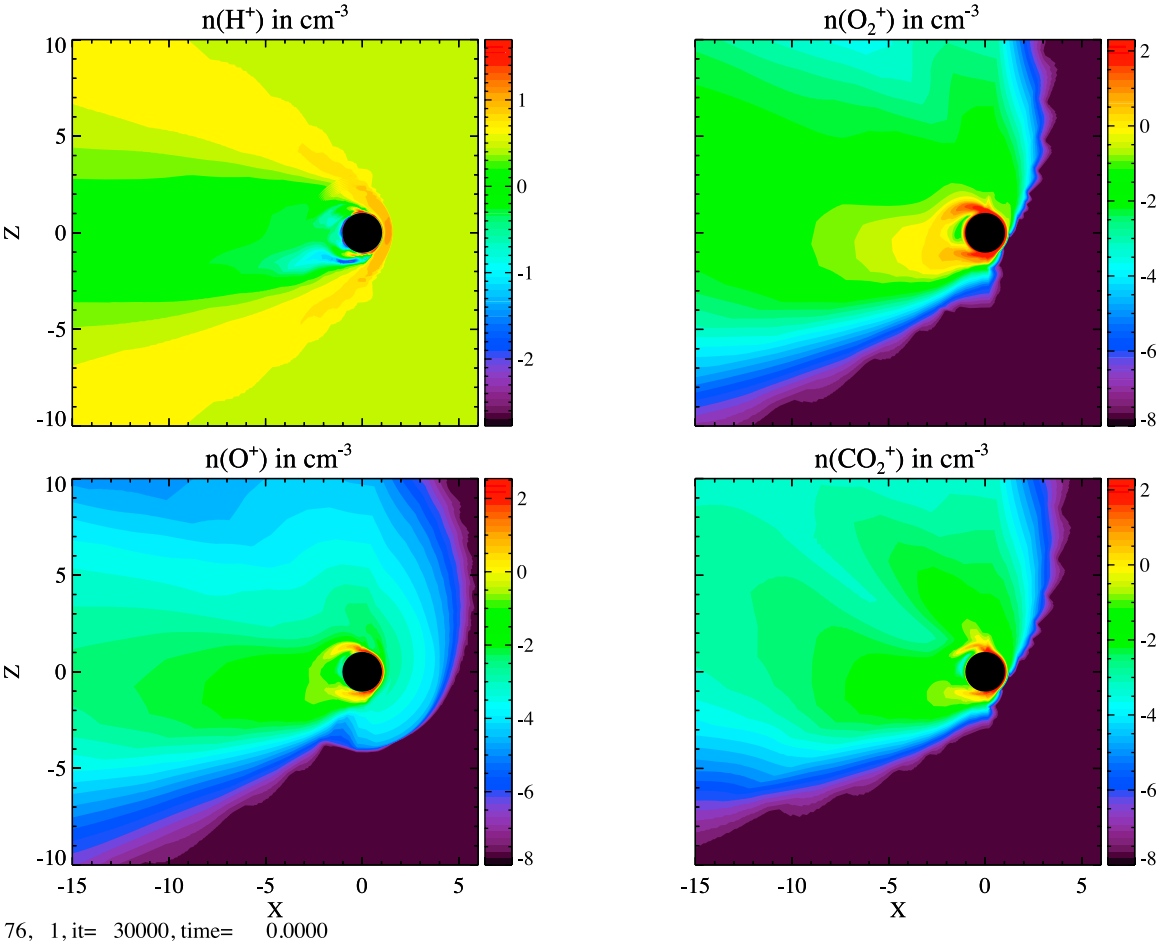

Figure 4. The calculated ion number densities in cm^{-3} in the X-Z plane for H^+, O_2^+, O^+, and CO_2^+. Note the use of a logarithmic scale (case 2).

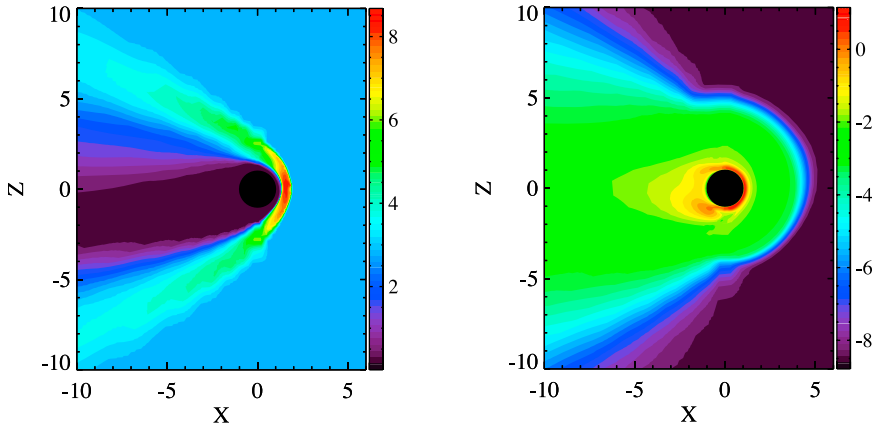

Figure 5. The calculated densities in cm^{-3} of the (left) solar wind and (right) ionospheric hydrogen. Note that the ionospheric hydrogen density is in a logarithmic scale unlike the solar wind hydrogen density, which is plotted using a linear scale for the sake of clarity.

[25] O_2^+ and CO_2^+ contour plots are quite similar, whereas O^+ has a different shape mainly due to the ionization of the neutral oxygen corona, which pushes the density jump outward. The hydrogen draping around Mars is barely visible since we do not distinguish between solar wind and ionospheric hydrogen. In order to observe the hydrogen properties more clearly, we introduced an additional hydrogen fluid and separated ionospheric and solar wind hydrogen. As a result, we observe as expected the formation of a sharper jump in the ionospheric hydrogen density and a cavity in the solar wind as shown in Figure 5.

4.2. Pressure

[26] Figure 6 shows the solar minimum subsolar pressure profile for case 3. $P_{thermal}$ is the total thermal pressure, P_B is the magnetic pressure. $P_{dynamic}$ is the dynamic pressure and P_{total} is the total pressure. As predicted, the presence of the crustal field pushes the magnetic pileup outward and increases its intensity. The bow shock separates the dynamic pressure and the thermal pressure dominated regions. The bow shock is located at 1.56 R_M, which is close to MGS observations [*Vignes et al.*, 2002] and slightly further out than the single-fluid model results [*Ma et al.*, 2004]. We can see the magnetic pileup boundary as we move from a thermal pressure to a magnetic pressure dominated region at 1.17 R_M. These pressure plots (Figures 6, 7, and 10) show an increasing magnetic pressure resulting in an increasing total pressure from about 1.2 R_M down to about 1.08 R_M. It must be remembered that when considering the competing forces in this region one must also consider the magnetic tension and gravitational forces. When all the relevant force components are taken into account the net force is approximately zero in this region.

[27] We also run simulations for the solar maximum case (case 4) so as to see whether the solar condition plays a role in the bow shock location as well in the shape of the pressure profiles. The main difference between solar minimum and solar maximum is different neutral profiles and ionization rates (not in the values of the solar wind conditions). This results in a more extended ion plume distribution around the body. Figure 7 shows the corresponding pressure profile. As observed in the single-fluid case [*Ma et al.*,

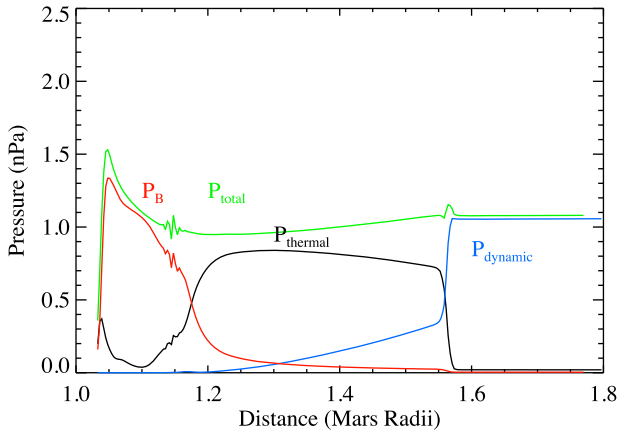

Figure 6. Pressure profiles along the Sun-Mars line in the dayside for solar minimum (case 3).

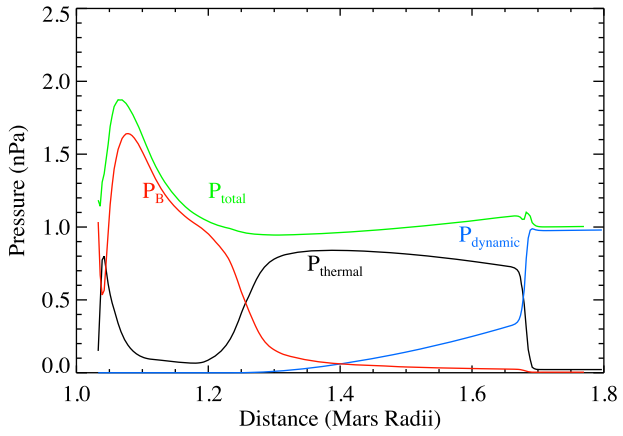

Figure 7. Pressure profiles along the Sun-Mars line in the dayside for solar maximum (case 4).

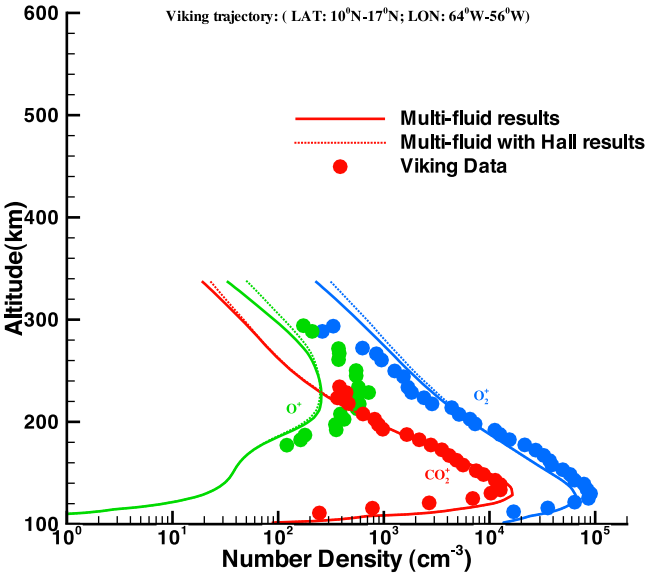

Figure 8. Comparison between Viking ion temperature measurements and the multifluid model results along the Viking trajectory (case 3).

2004], the solar maximum case has a bow shock and magnetic pileup boundary (MPB) further out from the body than in the solar minimum case. In Figure 7 we observe the bow shock at 1.67 R_M and the MPB at 1.26 R_M. This is consistent with observations along the subsolar line [*Vignes et al.*, 2000] plotted in Figures 2 and 3. The averaged terminator MPB and bow shock locations for case 4 are 1.37 and 2.54 R_M, respectively, which is also consistent with MGS observations [*Vignes et al.*, 2000].

4.3. Comparison to Data and Role of the Hall Effect

[28] Our new model has been validated by comparing it to the single-fluid model results and to observed values. We compare our solar minimum results (case 3) to the Viking observations by running a solar minimum simulation with the subsolar location taken to be at 99.4 west longitude and 25.3 north latitude in order to closely approximate the Viking conditions. The density and ion temperature results are shown in Figures 8 and 9, along with the Viking results [*Hanson et al.*, 1977].

[29] The agreement between the calculated and observed parameters in the region of the Viking measurements is similar to that obtained by the multispecies single-fluid model of *Ma et al.* [2004], which is not surprising given the fact that the same chemistry scheme and neutral atmosphere parameters were used in both set of calculations and transport processes are not very strong in the region under consideration. The agreement between the calculated and observed molecular ion densities is quite good. The model results for O^+ are noticeably lower than the measured values. However, we need to remember that the Viking mass spectrometer did not measure the atomic neutral density. Most of our current estimate of the O density came from fitting the measured O^+ density by adjusting the neutral O density in 1-D ionospheric models until a good fit was obtained [e.g., *Hanson et al.*, 1977; *Chen et al.*, 1978]. In order to compare our results with the single-fluid model results we used the same neutral density values selected by *Ma et al.* [2004] and we did not undertake a systematic study of adjusting the O density to get a best fit. However as a test, we did double our O densities in order to establish the kind of adjustments necessary and that gave us a very good fit to the observed O^+ densities.

[30] It is known that the transition between chemical equilibrium conditions to transport takes place around 200 km. In fact, in that region, and above the ionospheric peak, the plasma decreases with a scale height that is equal to approximately twice that of the major ionizable neutrals [cf. *Schunk and Nagy*, 2009]. The measured Viking CO_2^+ and O_2^+ scale heights are about 23 and 29 km and it is also the case for our calculated values. The exospheric neutral gas temperature has been measured by Viking [*Nier and McElroy*, 1977] to be about 185 K, giving a neutral scale height of about 10.4 and 28.5 km for CO_2 and O, respectively, which is consistent with the observed (Viking) and calculated (multifluid) data.

[31] The results presented so far were obtained neglecting the Hall effect in the magnetic field equation to highlight the asymmetries caused by the multifluid effect rather than the ones due to the decoupling of ions and electrons via the Hall effect. However, the Hall effect is available as an option in our code [*Ma et al.*, 2007; *Tóth et al.*, 2008] and has been included in some of our runs. As we can see in Figure 9, the addition of the Hall term does not modify our results significantly. The pressure profile shown in Figure 10 corresponds to the solar maximum case with the Hall effect included; we can only see a slight outward movement of the shock. A summary of the MPB and bow shock positions for different cases is shown in Table 3.

4.4. Escape Fluxes

[32] We also used our model to estimate the total escape fluxes at 6 Mars radii. Our results, given in Table 4, are

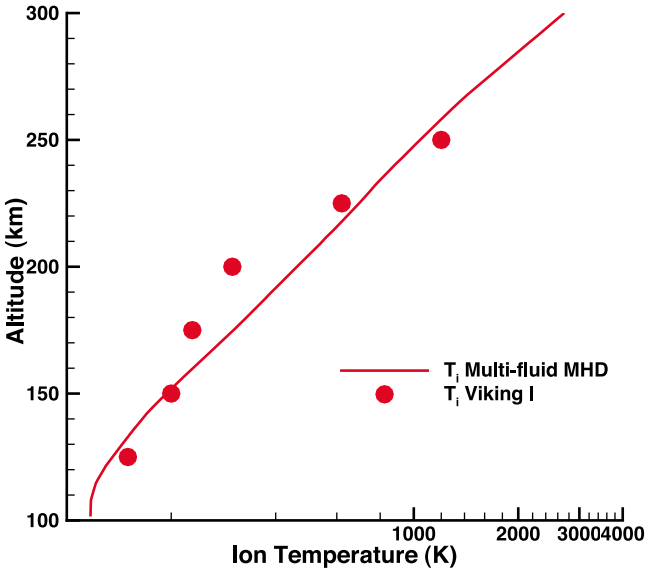

Figure 9. Comparison between Viking ion density measurements and the multifluid model results (with and without the Hall effect) along the Viking trajectory (case 3).

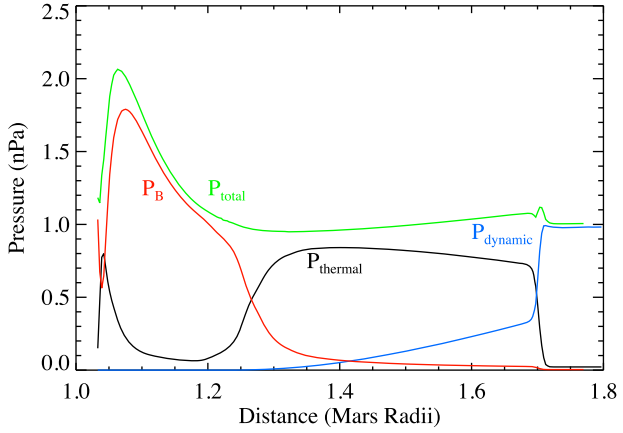

Figure 10. Pressure profiles along the Sun-Mars line in the dayside for solar maximum with the Hall effect.

somewhat different from the single-fluid model [*Ma et al.*, 2007]. One of the main differences between our two models is the higher O_2^+ escape flux compared to the escape rates of the other species. This might be due to the new dynamics observed through our model, in particular the existence of asymmetric plumes. Finally, our calculated total flux values are comparable but somewhat lower than the most recent measurement (3×10^{24} s^{-1}), from the ASPERA instrument carried by Mars Express [*Lundin et al.*, 2008].

5. Summary

[33] Our new multifluid MHD model of Mars gives very promising new results. It succeeds in describing new physical processes such as the density plumes and the asymmetries due to the decoupling of the ions, which could not previously be observed with the single-fluid model. At the same time, it verifies the observed bow shock locations and shows a reasonable fit to the data.

[34] We observe an asymmetric magnetic pileup in the X-Z plane resulting from the Lorentz force in the Z direction. The Lorentz force also affects the ion density distribution around the body in the same plane. The asymmetric density plume is a distinguishing feature for the heavy species (O^+, O_2^+, CO_2^+) and is a direct result of the decoupling of the ions as separate fluids. Our results are similar to results previously obtained by hybrid models [e.g., *Brecht*, 1997; *Brecht and Ledvina*, 2007; *Kallio et al.*, 2010], in regions where the simulations overlap. This work demonstrates that multifluid MHD models provide a good and credible way to study the interaction of fast moving plasmas with nonmagnetic solar wind bodies.

Table 3. Calculated Subsolar MPB and Bow Shock Positions for Solar Minimum and Solar Maximum With and Without Hall[a]

Solar Condition	Hall	MPB Location in R_M	Bow Shock Location in R_M
Solar minimum (case 3)	No	1.17	1.56
Solar minimum (case 3)	Yes	1.17	1.58
Solar maximum (case 4)	No	1.26	1.67
Solar maximum (case 4)	Yes	1.27	1.7

[a]The observed subsolar bow shock and MPB locations are 1.64 ± 0.08 R_M and 1.29 ± 0.04 R_M, respectively [*Vignes et al.*, 2000].

Table 4. Calculated Escape Fluxes (in s^{-1}) From the Multifluid Model

	O^+	O_2^+	CO_2^+	Total
Case 3	1.6×10^{23}	1.4×10^{24}	2.1×10^{23}	1.77×10^{24}
Case 4	7.7×10^{23}	9.0×10^{23}	1.7×10^{23}	1.84×10^{24}

[35] We ran our model for different configurations (cases 1–4) and we observed that changing to solar maximum conditions pushes the magnetic pileup boundary and the bow shock outward. This variability of both the bow shock and the MPB has been predicted by the multispecies single-fluid model and is now confirmed by our multifluid model. The Hall effect did not affect our results significantly.

[36] Our multifluid model gives reasonable escape fluxes and the density results compare reasonably well with the observations made by MGS and Viking data, thus validating our model. Our future plans are to add the electron fluid to our simulations by solving for the electron pressure and include thermal conduction in our equations.

[37] **Acknowledgments.** The authors wish to acknowledge the help of Tamas Gombosi. The work presented here was supported by NASA Earth and Space Science Fellowship NNX07AT34H and NSF grant ATM-0845133.

[38] Masaki Fujimoto thanks Hiroyuki Shinagawa and another reviewer for their assistance in evaluating this paper.

References

Acuna, M. H., et al. (1998), Magnetic field and plasma observations at Mars: Initial results of the Mars Global Surveyor mission, *Science*, *279*, 1676–1680.

Arkani-Hamed, J. (2001), A 50-degree spherical harmonic model of the magnetic field of Mars, *J. Geophys. Res.*, *106*, 23,197–23,208.

Bauske, R., A. Nagy, T. Gombosi, D. De Zeeuw, K. Powell, and J. Luhmann (1998), A three-dimensional MHD study of solar wind mass loading processes at Venus: Effects of photoionization, electron impact ionization, and charge exchange, *J. Geophys. Res.*, *103*, 23,625–23,638.

Brain, D., et al. (2010), A comparison of global models for the solar wind interaction with Mars, *Icarus*, *206*, 149–151, doi:10.1016/j.icarus.2009.06.030.

Brecht, S. (1997), Hybrid simulations of the magnetic topology of Mars, *J. Geophys. Res.*, *102*, 4743–4750.

Brecht, S. H., and S. A. Ledvina (2007), The solar wind interaction with the Martian ionosphere/atmosphere, *Space Sci. Rev.*, *126*, 15–38.

Chen, R. H., T. E. Cravens, and A. F. Nagy (1978), The Martian ionosphere in light of the Viking observations, *J. Geophys. Res.*, *83*, 3871–3876.

Fox, J., and K. Sung (2001), Solar activity variations of the Venus thermosphere/ionosphere, *J. Geophys. Res.*, *106*, 21,305–21,335.

Glocer, A., G. Tóth, Y. Ma, T. Gombosi, J.-C. Zhang, and L. M. Kistler (2009), Multifluid Block-Adaptive-Tree Solar Wind Roe-Type Upwind Scheme: Magnetospheric composition and dynamics during geomagnetic storms—Initial results, *J. Geophys. Res.*, *114*, A12203, doi:10.1029/2009JA014418.

Hanson, W. B., S. Sanatini, and D. R. Zuccaro (1977), The Martian ionosphere as observed by the Viking retarding potential analyzer, *J. Geophys. Res.*, *82*, 4351–4363.

Harnett, E. M., and R. M. Winglee (2003), The influence of a mini-magnetopause on the magnetic pileup boundary at Mars, *Geophys. Res. Lett.*, *30*(20), 2074, doi:10.1029/2003GL017852.

Harnett, E. M., and R. M. Winglee (2007), High-resolution multifluid simulations of the plasma environment near the Martian magnetic anomalies, *J. Geophys. Res.*, *112*, A05207, doi:10.1029/2006JA012001.

Kallio, E., K. Liu, R. Jarvinen, V. Pohjola, and P. Janhunen (2010), Oxygen ion escape at Mars in a hybrid model: High energy and low energy ions, *Icarus*, *206*, 152–163.

Ledvina, J. A., et al. (2008), Modeling and simulating flowing plasmas and related phenomena, *Space Sci. Rev.*, *329*, 143–189.

Lundin, R., S. Barabash, M. Holmström, H. Nilsson, M. Yamauchi, M. Fraenz, and E. M. Dubinin (2008), A comet-like escape of ionospheric

plasma from Mars, *Geophys. Res. Lett.*, *35*, L18203, doi:10.1029/2008GL034811.

Ma, Y., A. F. Nagy, I. V. Sokolov, and K. C. Hansen (2004), Three-dimensional, multispecies, high spatial resolution MHD studies of the solar wind interaction with Mars, *J. Geophys. Res.*, *109*, A07211, doi:10.1029/2003JA010367.

Ma, Y., et al. (2007), 3D global multi-species Hall-MHD simulation of the Cassini T9 flyby, *Geophys. Res. Lett.*, *34*, L24S10, doi:10.1029/2007GL031627.

Modolo, R., G. Chanteur, E. Dubinin, and A. P. Matthews (2006), Simulated solar wind plasma interaction with the Martian exosphere: Influence of the solar EUV flux on the bow shock and the magnetic pile-up boundary, *Ann. Geophys.*, *24*(12), 3403–3410.

Nier, A. O., and M. B. McElroy (1977), Composition and structure of Mars' upper atmosphere—Results from the neutral mass spectrometers on Viking 1 and 2, *J. Geophys. Res.*, *82*, 4341–4349.

Powell, K. G., P. L. Roe, T. J. Linde, T. I. Gombosi, and D. L. De Zeeuw (1999), A solution-adaptive upwind scheme for ideal magnetohydrodynamics, *J. Comput. Phys.*, *154*, 284–309.

Schunk, R. W., and A. F. Nagy (2009), *Ionospheres*, 2nd ed., Cambridge Univ. Press, New York.

Simon, S., G. Kleindienst, A. Boesswetter, T. Bagdonat, U. Motschmann, K.-H. Glassmeier, J. Schuele, C. Bertucci, and M. K. Dougherty (2007), Hybrid simulation of Titan's magnetic field signature during the Cassini T9 flyby, *Geophys. Res. Lett.*, *34*, L24S08, doi:10.1029/2007GL029967.

Spreiter, J. R., A. Summers, and A. Rizzi (1970), Solar wind flow past nonmagnetic planets—Venus and Mars, *Planet. Space Sci.*, *18*(9), 1281–1299.

Tanaka, T., and K. Murawski (1997), Three-dimensional MHD simulation of the solar wind interaction with the ionosphere of Venus: Results of two-component reacting plasma simulation, *J. Geophys. Res.*, *102*, 19,805–19,821.

Terada, N., H. Shinagawa, T. Tanaka, K. Murawski, and K. Terada (2009), A three-dimensional, multispecies, comprehensive MHD model of the solar wind interaction with the planet Venus, *J. Geophys. Res.*, *114*, A09208, doi:10.1029/2008JA013937.

Tóth, G., Y. J. Ma, and T. I. Gombosi (2008), Hall magnetohydrodynamics on block adaptive grids, *J. Comput. Phys.*, *227*, 6967–6984.

Tóth, G., A. Glocer, Y. Ma, D. Najib, and T. Gombosi (2009), Multi-ion magnetohydrodynamics, in *Numerical Modeling of Space Plasma Flows, Astronum-2009*, vol. 429, 213–218, Astron. Soc. of the Pac., San Francisco, Calif.

Tóth, G., et al. (2011), Adaptive numerical algorithms in space weather modeling, *J. Comput. Phys.*, in press.

Vignes, D., et al. (2000), The solar wind interaction with Mars: Locations and shapes of the bow shock and the magnetic pile-up boundary from the observations of the MAG/ER experiment onboard Mars Global Surveyor, *Geophys. Res. Lett.*, *27*, 49–52.

Vignes, D., M. H. Acuna, J. E. P. Connerney, D. H. Crider, H. Reme, and C. Mazelle (2002), Factors controlling the location of the bow shock at Mars, *Geophys. Res. Lett.*, *29*(9), 1328, doi:10.1029/2001GL014513.

Y. Ma, Institute of Geophysics and Planetary Physics, University of California, Los Angeles, CA 90095, USA.

A. F. Nagy, D. Najib, and G. Tóth, Department of Atmospheric, Oceanic and Space Sciences, University of Michigan, Ann Arbor, MI 48109-2143, USA. (dnajib@umich.edu)